The Astrophysical Journal Letters, 939:L21 (10pp), 2022 November 10 https://doi.org/10.3847/2041-8213/ac982a

Populations of Magnetized Filaments in the Intracluster Medium and the Galactic Center

F. Yusef-Zadeh[1], R. G. Arendt[2,3], and M. Wardle[4]
[1] Department of Physics and Astronomy, CIERA, Northwestern University, 2145 Sheridan Road, Evanston , IL 60207, USA; zadeh@northwestern.edu
[2] Code 665, NASA/GSFC, 8800 Greenbelt Road, Greenbelt, MD 20771, USA; Richard.G.Arendt@nasa.gov
[3] UMBC/CRESST 2
[4] School of Mathematical and Physical Sciences, Research Centre for Astronomy, Astrophysics and Astrophotonics, Macquarie University, Sydney NSW 2109, Australia; mark.wardle@mq.edu.au
Received 2022 September 9; revised 2022 October 6; accepted 2022 October 6; published 2022 November 2

Abstract

Magnetized radio filaments are found in abundance in the inner few hundred parsecs of our galaxy. Progress in understanding this population of filaments has been slow over the last few decades, in part due to a lack of detection elsewhere in the galaxy or in external galaxies. Recent highly sensitive radio continuum observations of radio galaxies in galaxy clusters have revealed remarkable isolated filamentary structures in the intracluster medium (ICM) that are linked to radio jets, tails, and lobes. The origin of this class of filaments is not understood either. Here, we argue that the underlying physical mechanisms responsible for the creation of the two populations are the same because of their similarities in morphology, spacing between the filaments, aspect ratio, and magnetic energy densities to the thermal pressure of the medium and that both populations have undergone synchrotron aging. These similarities provide an opportunity to investigate the physical processes in the interstellar medium (ISM) and ICM for the first time. We consider that the origin of the filaments in both the Galactic center and ICM is a result of the interaction of a large-scale wind with clouds, or the filaments arise through the stretching and collection of field lines by turbulence in a weakly magnetized medium. We examine these ideas in four radio galaxy filaments associated with four radio galaxies—IC 40B, IC 4496, J1333–3141, ESO 137–006—and argue that much can be understood in the future by comparing these two populations of filaments.

Unified Astronomy Thesaurus concepts: Fanaroff-Riley radio galaxies (526); Galactic center (565); Cosmic rays (329); Galaxy clusters (584); Intracluster medium (858); Interstellar magnetic fields (845)

1. Introduction

In the last few years, sensitive high-resolution radio continuum observations of galaxy clusters have begun to reveal a population of magnetized filamentary structures in their intracluster medium (ICM) (Shimwell et al. 2016; Ramatsoku et al. 2020; Condon et al. 2021; Fanaroff et al. 2021; van Weeren et al. 2021; Brienza et al. 2022; Giacintucci et al. 2022; Knowles et al. 2022; Rudnick et al. 2022). Discoveries of new structures in the ICM surrounding radio galaxies (RGs) are in large part due to recent advances in broadband correlators installed on radio telescopes, providing remarkable brightness sensitivity and dynamic range with exquisite details at $\sim 6''$ spatial resolution. A striking aspect of the appearance of these long and narrow isolated filaments is that they are not located within the radio lobes, the tails of radio galaxies, or associated with the radio core of the galaxy (Lane et al. 2002; Hardcastle et al. 2019). The filaments are detected outside radio galaxies but linked to radio lobes and jets with a wide range of angles to the orientation of radio jets or the lobes. The nature of this new phenomenon, which appears to be common in high-dynamic-range images of radio galaxies, had not been appreciated or predicted in previous studies due to the lack of sufficient surface brightness sensitivity and angular resolution, particularly at lower frequencies.

Closer to home, in the vastly different environment of the Galactic center (GC), radio observations have uncovered a population of magnetized radio filaments with linearly polarized synchrotron emission tracing cosmic-ray activity throughout the inner few hundred parsecs of the galaxy (Yusef-Zadeh et al. 1984, 2004; Liszt 1985; Bally & Yusef-Zadeh 1989; Gray et al. 1991; Haynes et al. 1992; Staguhn et al. 1998, 2019; Lang et al. 1999; LaRosa et al. 2001, 2004; Nord et al. 2004; Law et al. 2008; Pound & Yusef-Zadeh 2018; Arendt et al. 2019). MeerKAT observations have provided a remarkable mosaic of the inner few degrees of the Galactic center revealing hundreds of radio filaments, housed within a $\sim$400 pc bipolar radio bubble filled with thermal X-ray gas that surrounds the Galactic center (Heywood et al. 2019, 2022; Yusef-Zadeh et al. 2022a, 2022b). H_3^+ measurements toward the Galactic center have quantified the cosmic-ray ionization rate to be 10^2 to 10^3 times greater than across the rest of the galaxy (Oka et al. 2005, 2019). This high ionization rate led to the interpretation that cosmic rays drive the wind, producing the radio bubble (Yusef-Zadeh & Wardle 2019).

In spite of decades of studying the GC filaments, a good understanding of these structures is still lacking. The emerging population of extragalactic radio filaments appears to have remarkably similar properties to the radio filaments in the GC. The comparison of the generic properties of both populations provides an opportunity to gain insight into the origin of both populations. Here, side-by-side images of four examples of GC and ICM filaments are displayed in Section 2 to illustrate their similar morphologies, followed by a discussion of the properties that are common in two populations of GC and ICM filaments in Section 3. We then compare the physical parameters of the two populations of filaments in Section 4 and discuss their implications for models of their structure and origin in Section 5.

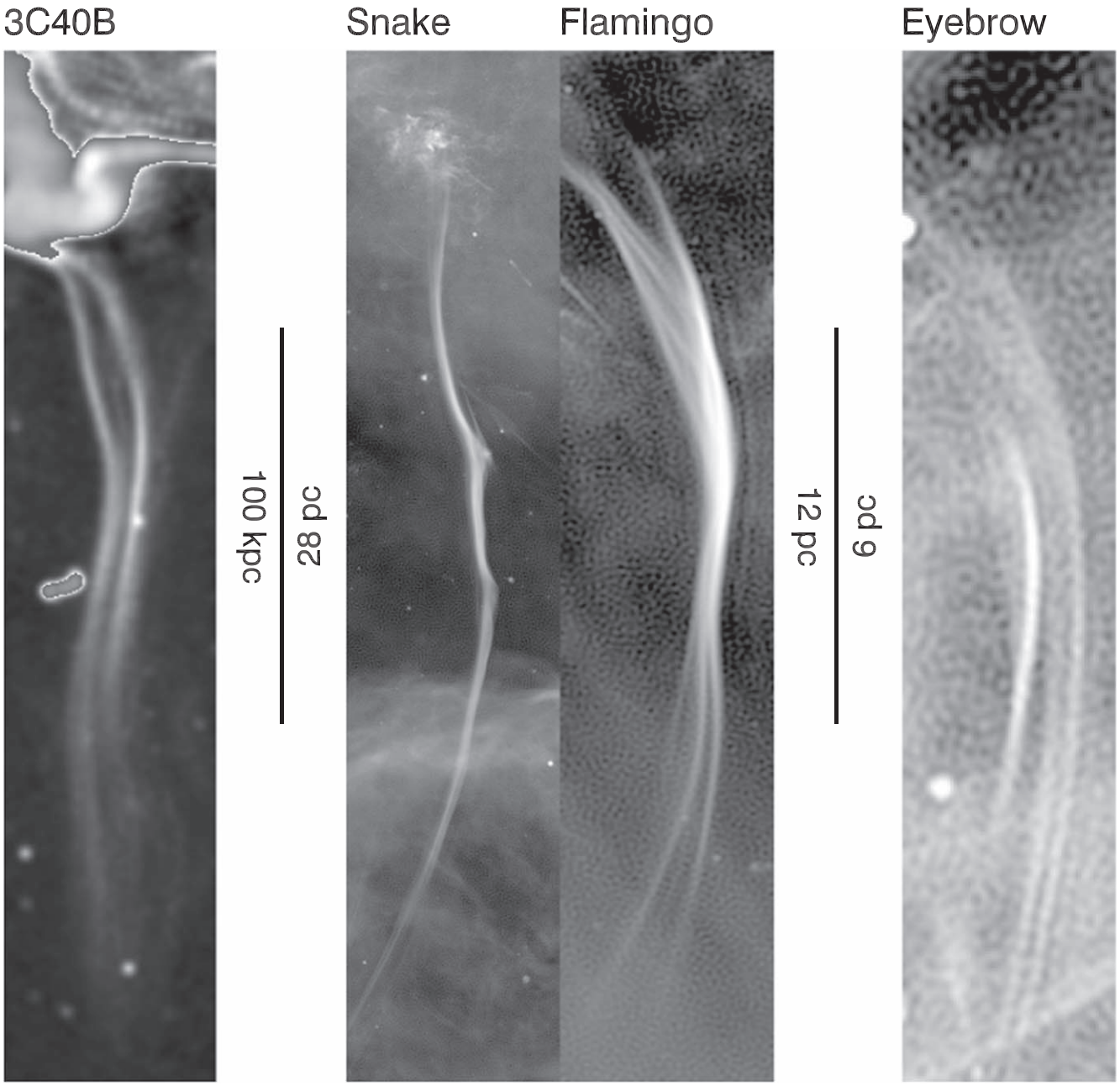

Figure 1. Left: a grayscale MeerKAT image of the radio galaxy 3C 40B and its long filaments (Rudnick et al. 2022). The filaments are connected to a portion of the jet shown at the top of the panel. Right: the three panels to the right display three groups of GC radio filaments based on a 4″ resolution MeerKAT mosaic of the GC at 1.28 GHz (Heywood et al. 2022), discussed in detail in Yusef-Zadeh et al. (2022b). The intensity I (Jy beam^{-1}) scales are, for 3C 40B, $-4 < \log(I) < -1.4$ for the bright emission, and $-1 \times 10^{-4} < I < 7.8 \times 10^{-4}$ for the fainter emission; Snake, $-4 < \log(I + 3 \times 10^{-4}) < -2.33$; Flamingo, $-4.3 < \log(I + 3 \times 10^{-4}) < -2.3$; and Eyebrow, $-4.3 < \log(I + 5 \times 10^{-4}) < -3$.

2. GC versus ICM Filaments: Four Examples

The GC filaments are rich in their morphological variety and details as well as being abundant in the inner few hundred parsecs of the Galactic center. ICM filaments are being revealed in high-dynamic-range images of radio galaxies and their surrounds. We have selected a subset of GC filaments based on their similar morphology to ICM filaments. The comparison of a limited number of ICM filaments with a large number of GC filaments offers an opportunity to advance our understanding of the origin of the filaments and to probe the magneto-ionized media of the GC and ICM. We examine below the morphology and properties of filaments associated with four RGs and compare them with seven GC filaments.

2.1. C40B in A194 versus G359.132–0.296 (the Snake), G359.808+0.130 (the Flamingo), and G359.717+0.228 (the Eyebrow)

Figure 1 displays a comparison of the filamentary structures associated with the radio jet of 3C 40B and three morphologically similar groups of filaments identified in the GC (Yusef-Zadeh et al. 2022b). 3C 40B is a radio galaxy at a distance of ∼75.5 Mpc, embedded in the poor cluster environment Abell

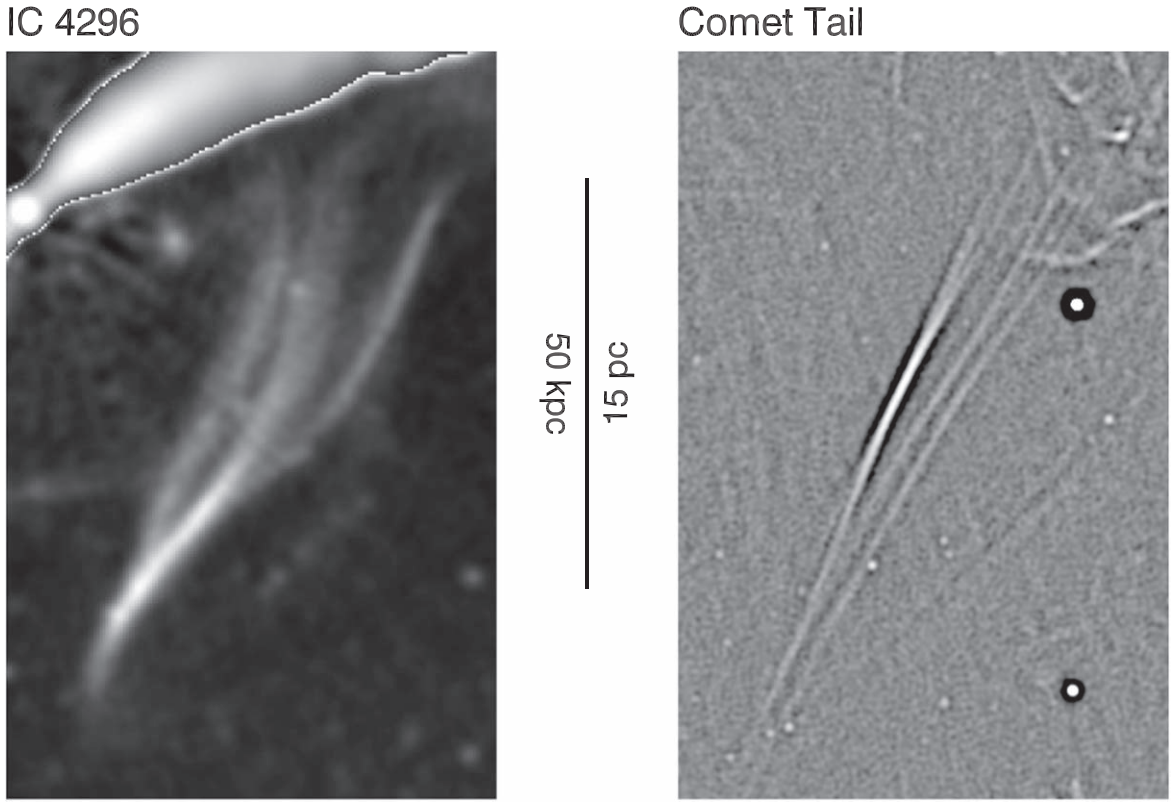

Figure 2. Left: a grayscale MeerKAT image of the core and its radio jet (top of the panel) and the filaments (center of the panel) of IC 4296, an elliptical radio galaxy, is displayed (Condon et al. 2021). Because of the strong surface brightness of the core and the jet compared to the filaments, different color tables were applied. Right: a MeerKAT filtered image of the comet tail as discussed in Yusef-Zadeh et al. (2022b). The intensity I (Jy beam^{-1}) scales are, for IC 4296, $-4 < \log(I) < -1.2$ where $I > 3.6 \times 10^{-4}$ and $-4 \times 10^{-5} < I < 3.6 \times 10^{-4}$ for the fainter emission, and the comet tail, $-5 < \log(I + 3 \times 10^{-4}) < -4$.

194 (A194; Knowles et al. 2022), which has recently been studied in detail (Rudnick et al. 2022). Two remarkable filaments emerge from a deviated region of the jet and run parallel to each other as they bend together with two different curvatures leading to diffuse ends. The angular spacing between the filaments is $\sim 30''$ ($\sim$11 kpc), their widths range between 0.85 and 2.8 kpc, and both have an extent of $\sim$220 kpc (Rudnick et al. 2022). The filaments show signs of physical interaction with a region of the jet that is highly bent, suggesting a scenario in which a cloud is crossing the jet and the filaments are then dragged from the interaction site (Rudnick et al. 2022).

The Snake has a length of $\sim 30'$ ($\sim$70 pc), is one of the longest in the Galactic center, and is characterized by two kinks and three different curvatures along its length. Another two examples of GC filaments are the groups known as the Flamingo and the Eyebrow. The Flamingo shows multiple filaments with similar curvatures and the Eyebrow consists of two parallel filaments with the same curvature suggesting that they are associated with each other.

The morphology of the four filament groups shown in Figure 1 is similar to each other to the extent that it is difficult to distinguish which one is in a galaxy cluster based on appearance alone. The systems of filaments in the GC and 3C 40B have similar morphologies, surface brightnesses, length-to-width ratios, and angular spacings. What is remarkable is that the ICM filaments in 3C 40B are $\sim$7000 times longer than nonthermal filaments (a.k.a. NTFs) in the GC with a coherent magnetic structure, steepening spectral index, and streaming cosmic-ray particles over such a large distance (Rudnick et al. 2022), and yet they show similar physical characteristics.

The ranges of the spectral indices are $\alpha = [-0.60, -0.79]$ for the Snake, $\alpha = [-0.80, -1.05]$ for the Flamingo, $\alpha = [-0.51, -0.76]$ for the Eyebrow (Yusef-Zadeh et al. 2022b). These estimates of the spectral index are made along individual filaments. The GC spectral index values are all flatter than the spectral indices of the filaments in 3C 40B, which have a mean value of $\alpha \sim -2$ and steepen from -1.3 to -2.5 with distance from the jet.

The equipartition magnetic field of GC filaments ranges between 20 and 100 μG (for a cosmic-ray proton to electron ratio of $p/e = 1$), which is much higher than that of 3C 40B with the magnetic field of 2–7 μG. The equipartition magnetic field of the Snake has a maximum of $\sim$0.1 mG and decreases away from the Galactic plane (Yusef-Zadeh et al. 2022a). Furthermore, the direction of the magnetic field runs along the 3C 40B and the Snake filaments. (The magnetic field directions of the Flamingo and Eyebrow are unknown).

2.2. Radio Galaxy IC 4296 versus G359.992–0.572 (the Comet Tail)

IC 4296 is a low-luminosity elliptical galaxy in cluster A3566 at a distance of 50 Mpc (Condon et al. 2021), as shown in Figure 2. A sensitive radio image of this galaxy shows a remarkable group of three filaments with an angular spacing of $\sim 20''$ (called threads in Condon et al. 2021) that appear to converge to a point (Figure 2, left), as showin in Figure 2. The projected lengths and widths of the filaments are $\sim$50 and

$\sim$2 kpc, respectively, with a surface brightness of $\sim$0.1 mJy per $\sim 7\farcs6$ beam (Condon et al. 2021; Figure 2, left panel). This group of filaments lies to the south of the western radio jet where the jet shows a wiggle, thought to be due to Kelvin–Helmholtz (KH) instability (Condon et al. 2021). These authors suggest that relativistic electrons escape from the jet where there is KH instability along the radio jets (Condon et al. 2021). There is also a single isolated filament with a different position angle that arises from the eastern jet. One puzzle is that the spectral index of the filaments steepens from $\alpha \sim -1$ to -1.5 closer to the injection point of the radio jet.

The GC grouping of the comet tail consists of six linear structures that resemble a fragmented comet tail (Figure 2, right panel). Some of the filaments branch out into fainter components. The spectral index of individual filaments varies and shows steep spectra in the range $[-1, -1.8]$. There is a trend where the GC filaments with steeper spectral indices lie at high latitudes (Yusef-Zadeh et al. 2022a). The comparison indicates similar morphology and steep spectral indices in both the comet tail and IC 4296 filaments.

2.3. The Core of the A3562 Galaxy Cluster versus G359.411–0.709 (the Feather)

Figure 3(a) shows a radio image of the core of the A3562 galaxy cluster at a distance of $\sim$200 Mpc (Giacintucci et al. 2022). A linearly polarized filament with a length of 50 kpc runs perpendicular to the end of the tail of the radio galaxy J1333–3141. The filament that arises from the region where the jet terminates is distorted before it splits into two components (Giacintucci et al. 2022). The splitting occurs 60 kpc away from the radio tail. The mean spectral index of the filament is $\alpha \sim -1.5$.

For comparison we show in Figure 3(b), a striking GC filament, the Feather, which splits into a two-pronged forked filament with the junction at the location of a compact source G359.416–0.706 with a possible stellar counterpart detected at IR (Yusef-Zadeh et al. 2022a, 2022b). The compact source is suggested to be an obstacle that splits the bright filament into two parallel, fainter components with steeper spectral index values. The comparison noted in Figure 3 provides another example that radio filaments in both classes of Galactic and extragalactic filaments break up into multiple components, suggestive of a flow along the filaments that splits into two components as it runs into an obstacle.

2.4. ESO 137–006 versus G359.484+0.1122 (the Bent Harp)

Figure 4(a) shows a remarkable group of filaments linked to the radio lobes of ESO 137–006, a luminous radio galaxy in the Norma galaxy cluster at 70 Mpc from us (Ramatsoku et al. 2020). The wide-angle tail morphology of this radio galaxy includes multiple straight and bent filaments extending from the eastern lobe toward the western lobe. The longest straight filaments act as a bridge connecting the two radio lobes. In addition, a number of semiregularly spaced filaments are noted to the south of the lobes. The length and width of the longest filament are 80 kpc and 1.2 kpc, respectively, with an aspect ratio (length:width) of 67 (Ramatsoku et al. 2020). The mean spectral index of the filaments, $\alpha \simeq -2$, is similar to the spectral indices of the lobe from which they emerge. The western half of the galaxy is completely surrounded by diffuse X-ray emission. The western lobe is also highly distorted where diffuse and filamentary structures are present. The filaments bridging the lobes, with similar morphology to the above three examples, arise from a region where the jet is expanding into the lobe.

G359.484+0.1122 consists of five regularly spaced filaments with the appearance of a bent harp (Thomas et al. 2020; Yusef-Zadeh et al. 2022b). A trend was noted between the length of the filaments and their brightness as well as with the steepening of the spectral index in the range between $[-1.3, -1.0]$ (Yusef-Zadeh et al. 2022b).

The longest and straightest filament in ESO 137–006 (bridging the radio lobes) appears like many straight GC filaments running perpendicular to the Galactic plane (Yusef-Zadeh et al. 2022b). The Bent Harp is one group of GC filaments with a resemblance to the ICM structures in ESO 137–006. Unlike the filaments of ESO 137+006, the Bent Harp is not connected to any obvious sources of cosmic rays.

3. General Physical Properties

Galactic and extragalactic filaments are produced in totally different environments, namely, the nucleus of a normal galaxy and the intracluster medium. Their length scales, energy densities, and other characteristic parameters differ by orders of magnitude. In spite of these differences, we argue that similar processes operate in both systems motivated by their similar morphology and the similar dimensionless ratios of their physical parameters. We will examine and compare four examples of GC and RGs in the next section, following the common physical characteristics, as described below.

1. There is a remarkable similarity in the morphological details of the GC and ICM filaments despite their distances differing by a factor of $\sim 10^3$–10^4. Both classes of filaments are narrow and long with typical aspect ratios ranging between 10 and 50, assuming that the widths of the filaments are resolved. The filaments show bending and wiggles along their lengths and have similar surface brightness roughly ranging between 0.01 and 0.1 mJy beam^{-1}.
2. Both classes of filaments appear either as single isolated filaments or multiple filaments grouped together. Some of the apparently single filaments of the GC are found to consist of bundles of filaments in higher $\sim 1''$ resolution VLA observations. Many filaments in groupings are approximately equally separated from each other and run parallel to each other, giving a harp-like appearance. Filaments in some groupings converge to a point or to an extended source. Groups of filaments shift sideways together, changing direction coherently, implying that they are parts of the same system of filaments with a similar origin.
3. The mean spacings between parallel filaments in a given GC grouping peaks at $\sim 16''$ (Yusef-Zadeh et al. 2022b). There is a limited number of groups of ICM filaments but they show regular spacing between parallel filaments, as noted in numerous groups of GC filaments. In the case of 3C 40B, the spacing between two parallel filaments is $\sim 30''$ (Rudnick et al. 2022). We expect the spacing-to-length ratio of ICM and GC filament to be similar to each other if similar processes operate in both systems.
4. Both systems of GC and ICM filaments trace synchrotron emission from cosmic-ray electrons. They both show a

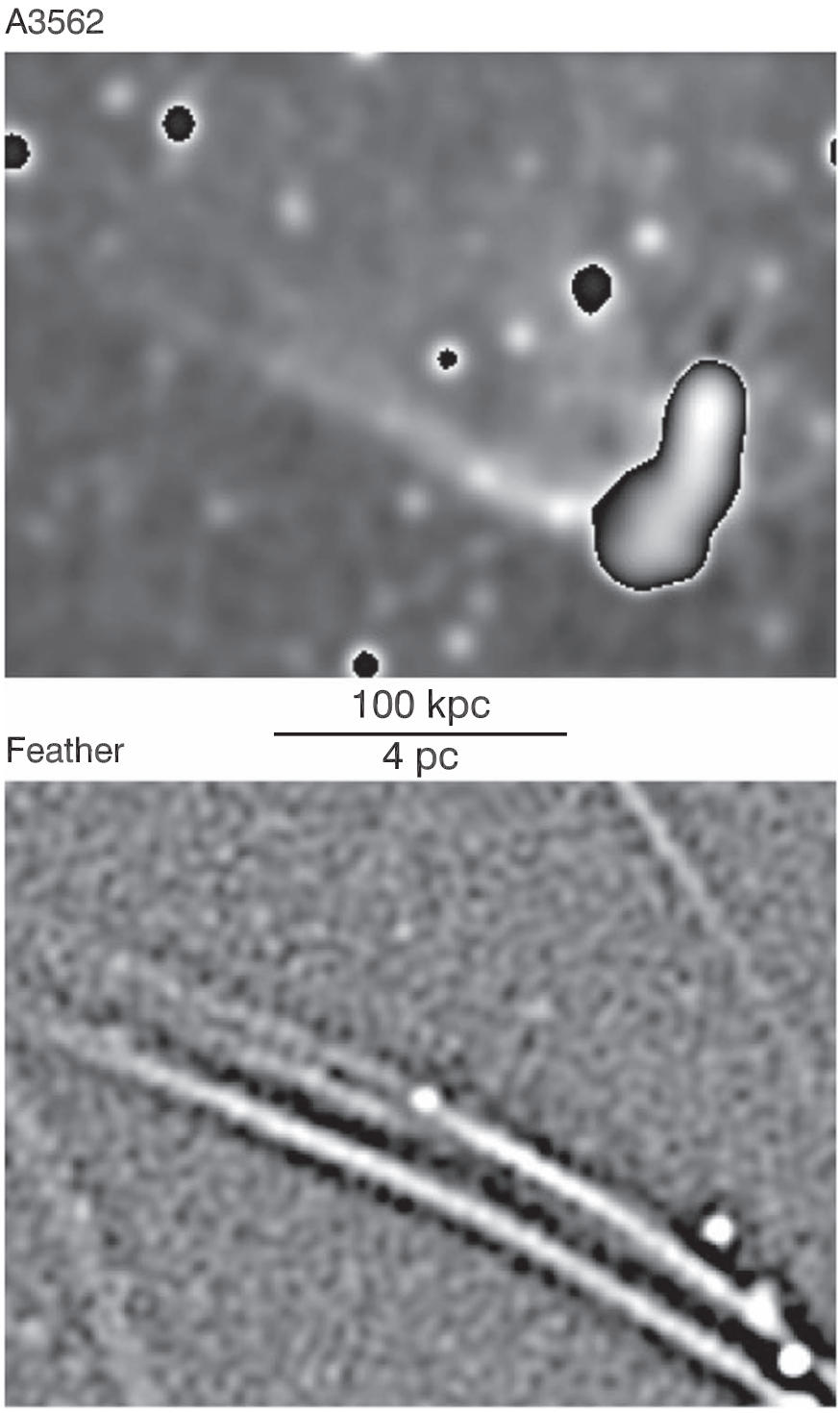

Figure 3. Top (a): a MeerKAT image of the galaxy cluster A3562 (Giacintucci et al. 2022) convolved with a Gaussian kernel with FWHM $\sim 10\farcs3$. Bottom (b): a portion of the Feather filament where the filament splits into two fainter components at a compact source (Yusef-Zadeh et al. 2022b). The intensity I (Jy beam^{-1}) scales are listed as follows: Feather: $-4.7 < \log(I + 3 \times 10^{-4}) < -4.3$; A3562: $-4 < \log(I) < -2$ where $I > 7\times 10^{-5}$ and $-2 \times 10^{-5} < I < 7 \times 10^{-5}$ for fainter regions.

high percentage of polarization, $\sim$50%, revealing ordered magnetic fields (B) running along the filaments. The orientation of the field is expected from velocity shear at the interface between the ICM filaments and the ambient gas in the ICM (Condon et al. 2021).

5. The mean magnetic field strengths along the GC filaments range between $\sim$100 and 400 μG depending on the assumed ratio of cosmic-ray protons to electrons (p/e). The magnetic field of ICM filaments is typically estimated to be a few microgauss, 50–100 times smaller. The low magnetic field of ICM filaments is expected because the filaments have a large depth L and old if steep spectral index, where flux density $S_\nu \propto \nu^\alpha$, is an indication of the age of cosmic-ray electrons. The weaker

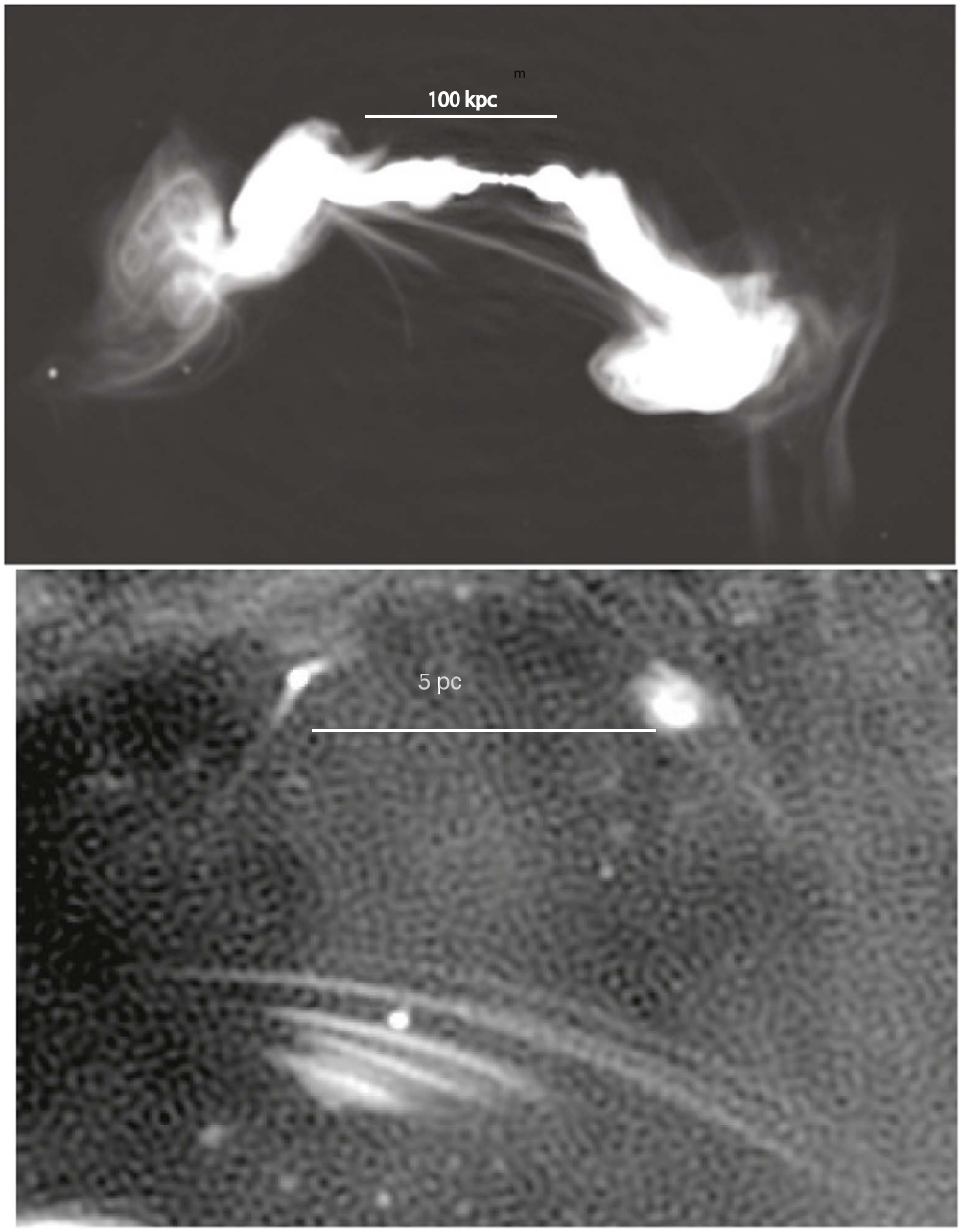

Figure 4. Top: a MeerKAT image of ESO 137–006 galaxy in the Norma galaxy cluster (Ramatsoku et al. 2020). The beam FWHM is $\sim 10''.7'' 62 \times 7'' 29$. Bottom: a portion of the Bent Harp filament showing multiple parallel filaments (Yusef-Zadeh et al. 2022b). The intensity I (Jy beam^{-1}) scale for the Bent Harp is $-3.8 < \log(I + 3 \times 10^{-4}) < -3$.

magnetic field in the ICM filaments implies long cooling timescales, which scale as $B^{-3/2}$ for observations at a fixed frequency.

6. The mean spectral indices of the GC filaments are steeper than supernova remnants (SNRs; $\alpha \sim -0.62$) with a value of $\alpha \sim -0.8$. Furthermore, a trend is noted in the steepening of the spectral index as a function of absolute Galactic latitude but not necessarily for typical GC filaments (LaRosa et al. 2000; Yusef-Zadeh et al. 2022a). With a limited number of ICM filaments, the typical spectral indices appear steeper than GC filaments, which is not surprising given the vastly longer timescales. In addition, the GC filaments show a number of filaments, such as the radio Arc near $l \sim 0.^{\circ}2$, with a relatively flat spectral index (Heywood et al. 2022; Yusef-Zadeh et al. 2022a).
7. In some ICM filaments, the radio lobes and tails of radio galaxies appear to provide an injection of cosmic-ray particles to illuminate radio filaments. However, the sources of particle injection in the GC filaments have not been well established. Recent MeerKAT measurements indicate a number of compact radio sources located at one or another end of the GC filaments. This suggests that compact radio sources are potentially responsible for the injection of cosmic-ray particles into radio filaments or acting as interfaces to collimate cosmic-ray-driven winds.
8. Diffuse thermal X-ray gas and diffuse nonthermal radio emission in the interstellar medium (ISM) of the GC and

Table 1
The Physical Characteristics of the Galactic Center and Radio Galaxy Filaments

Physical Parameters	Galactic Center Filaments	Radio Galaxy Filaments
length (pc)	[4, 60]	10^{3-5}
typical width (pc)	0.5	few$\times 10^3$
typical aspect ratio	[10, 100]	[10, 70]
magnetic field strength (mG)	[0.1, 0.6]	few$\times 10^{-3}$
spectral index (α)	~ -0.8 (mean) $[-2, 0]$	$[-2, -1]$
surface brightness (mJy beam^{-1})	[0.01–10]	[0.01, 10]
spacing between filaments (pc)	$\sim$0.7 mean [0.4, 1.2]	[10–20]$\times 10^3$

ICM of RGs suggest another similarity in the physical conditions of these environments. In addition, there is evidence of a high cosmic-ray ionization rate from H_3^+ studies of the Galactic center region.

4. The Origin of Two Populations of Filaments

The previous sections described the overall physical properties of a subset of ICM and GC filaments as members of two populations of magnetized radio filaments. There are hundreds of radio filaments found in the GC at a similar distance. A statistical study characterizing the mean properties of the spectral index, the equipartition magnetic field, and the spacing between the filaments and surface brightness is based on MeerKAT data at 1.28 GHz (Yusef-Zadeh et al. 2022a, 2022b). The physical parameters of GC and ICM filaments are listed in columns 2 and 3, respectively, of Table 1. In this table, the range and mean values of the length, width, magnetic field strength, surface brightness, and spacing between the filaments are given. The lengths of the GC filaments follow a power-law distribution (F. Yusef-Zadeh et al. 2022, in preparation). At present, only a handful of ICM filaments are known, thus there are not any sufficient measurements to do statistics beyond simple means. This is because ICM filaments require high-dynamic-range images to uncover faint magnetized filaments, and only limited observations are presently available. The GC filaments have a wide range of surface brightnesses with many more fainter filaments. The faint end is cut off by limited sensitivity. We recognize that the ICM filaments detected so far quite likely are the most prominent members of a larger population, with many fainter filaments yet to be detected.

4.1. Physical Parameters of GC and ICM Filaments

We compare the measurements and estimates of the physical characteristics of the two populations of filaments at the GC and in the ICM of galaxy clusters, as tabulated in Table 1, to explore the implications for the formation of the magnetic structures and the source of the ultrarelativistic electrons responsible for the observed radio emission. While the filament length scales and magnetic field strengths differ by orders of magnitude, it is their respective dimensionless ratios of timescales and length scales that should be compared. This allows us to examine whether the underlying physical mechanisms responsible for the creation of the two populations are similar. In particular, we are interested in the mechanisms responsible for creating magnetized filaments and for accelerating the relativistic electrons.

First, the morphological parameters of the two populations of filaments are similar: the aspect ratios are $\sim$30:1, there are multiple parallel filaments, splitting into a two-pronged fork, and bending and spacing between the filaments. The filaments appear in parallel bundles or to converge toward a point in both populations with a spacing of a few filament widths. These similarities are hardly surprising, given that the motivation behind making this comparison is that structures show a remarkable resemblance in the two environments, as shown in Figures 1–4.

Second, the filaments' magnetic fields are estimated to be of order 100 and 3 μG in the GC and ICM, respectively. Their corresponding magnetic energy densities, $B^2/8\pi \approx 3 \times 10^6$ and 3×10^3 cm^{-3} K, are comparable with or lower than the thermal pressure of the medium in which they are embedded. These characteristics suggest that the filaments are confined by the thermal pressure of the external medium. This is supported in the case of the filaments in A194 and IC 4296 (Condon et al. 2021; Rudnick et al. 2022), where the X-ray surface brightness of the intracluster medium is reduced along the filament, consistent with the exclusion of hot gas from the filament's interior. In the case of GC filaments, high external cosmic-ray energy density inferred from H_3^+ measurements contributes to the confinement of the GC filaments (Yusef-Zadeh & Wardle 2019).

Third, the spectral index values are steeper for ICM filaments than the mean spectral index of the GC filaments, as given in Table 1. Both systems of filaments also show steepening of the spectral index along individual filaments. The relativistic electron populations responsible for the observed synchrotron emission at 1.2 GHz have steep spectral indices and show a high percentage of linear polarization based on sensitive observations for both the GC and ICM filament populations.

For the equipartition field strengths mentioned above, the characteristic energy of the electrons dominating the emission at 1.2 GHz is $E = (4\pi m_e c\nu/3eB)^{1/2}\, m_e c^2 \approx 0.9$ and 5 GeV, respectively. The synchrotron power radiated by an ultra-relativistic electron of energy $E = \gamma m_e c^2$ is $\dot{E} = 2\sigma_T c\gamma^2 B^2/4\pi$, where for simplicity we have assumed a 90° pitch angle. Then, the synchrotron loss timescale $t_s = E/\dot{E} \approx 0.9$ or 200 Myr for the GC or IC filaments, respectively. As electron acceleration mechanisms tend to produce electrons with an E^{-2} energy spectrum and hence a $\nu^{-0.5}$ synchrotron spectrum, the steepness of the observed spectra implies that the filament ages are longer than the synchrotron lifetimes given above. In addition, the ages cannot be too much more than this because the filaments would rapidly become faint. Thus, the synchrotron lifetimes give a rough idea of the age of the filaments and impose a requirement on the cosmic-ray electron transport mechanism that must be able to distribute relativistic electrons along the observed filament lengths on this timescale.

4.2. Transport of Cosmic-Ray Electrons: Diffusion Versus Streaming

The disparate synchrotron loss timescales need to be placed in context. For source models involving acceleration or injection of relativistic electrons at a localized site, they impose a requirement to be able to transport the electrons via diffusion or streaming from the injection site throughout the observed filament lengths $L \sim 30$ pc and 100 kpc for the GC and ICM populations, respectively.

If transport is by diffusion, then the diffusion timescale $L^2/\kappa \lesssim t_s$ so the diffusion coefficient $\kappa \gtrsim L^2 t_s \sim 3 \times 10^{26}$ and 2×10^{31} cm^2 s^{-1}, respectively, implying mean free paths $l = 3c/\kappa \sim 0.01$ and 570 pc. The required diffusion is plausible for GC filaments with $L \lesssim 30$ pc but seems rather large in the case of the ICM filaments (Rudnick et al. 2022) as well as GC filaments, such as the Snake, with lengths $L \gtrsim 30$ pc. (see Figure 1).

The alternative to diffusion is that the cosmic-ray pressure is sufficient to allow them to stream along the magnetic field lines, in which case scattering by self-generated waves limits the streaming to the Alfvén speed, v_A. The requirement to populate the entire filament length then implies that $L/v_A \lesssim t_s$, i.e., $v_A \gtrsim L/t_s \sim 30$ and $\sim$600 km s^{-1} for the GC and ICM filaments, respectively. The density of the ionized thermal plasma present within the filaments is unknown, but we can usefully estimate the maximum density able to yield the required Alfvén speeds, using the characteristic field magnetic strengths $B \sim 100$ and 3 μG for the two populations. This implies that the thermal electron density $n_e \lesssim 3 \times 10^{11}$ and 8×10^5 cm^{-3} for the GC and ICM filaments, respectively. These upper limits clearly exceed any plausible value in each of the environments by orders of magnitude, so we can conclude another similarity in parameter space between the two populations that streaming would be able to transport electrons from their injection site along the entire length of the observed filaments.

4.3. ICM and GC Filament Models

Models of ICM filaments benefit from the fact that there is an obvious reservoir of cosmic-ray particles in jets, lobes, and mini radio halos (Brunetti & Jones 2014) that can be injected into filaments. For example, the filaments of the radio galaxy IC 4296 are thought to originate where helical KH instability disrupts the flow of the radio jet followed by the relativistic particles feeding the filaments (Condon et al. 2021). One puzzle is why the spectrum flattens instead of steepening while moving away from the presumed injection point at the end of the cometary structure's tail toward the convergence point of the filaments. One possible explanation for this is that the injected particles' pitch angle would tend to increase to conserve the magnetic moment $p_\perp/B$ as they spiral along the converging field lines. This mechanism relies on the initial pitch angle of the injected particles being anticorrelated with energy and the pitch-angle scattering to be ineffective in isotropizing the pitch-angle distribution.

In the case of the A3562 galaxy cluster, it has been suggested that the tail of the radio galaxy is interacting with a tangential wind blown in the direction along the filaments (Giacintucci et al. 2022). An alternative to this picture is a scenario in which the cosmic-ray electrons injected from the tail feed cluster magnetic field lines (Giacintucci et al. 2022). In another model, cosmic-ray electrons associated with two parallel filaments of 3C 40B are injected from a region where the jet is highly distorted (Rudnick et al. 2022). In particular, an impact between a moving dense cloud and the jet is expected to distort the shape of the jet as the magnetic field lines are dragged away from the site of the interacting jet (Rudnick et al. 2022). Another remarkable object is source C in A2256 with its extremely narrow and long tail. This unusual source is considered to be a one-sided radio jet. However, it has a very similar morphology to GC radio filaments. Lastly, the collimated synchrotron filaments in ESO 137–006 could be due to the interaction of the magnetic fields of the radio lobes with the magneto-ionic plasma of the intracluster medium (Ramatsoku et al. 2020).

4.4. Scenarios for the Origin of the ICM and GC Filaments

In GC and ICM populations, there are two broad scenarios that could potentially explain how magnetic filaments are formed. Both scenarios posit the amplification and organization of an initially weak magnetic field in the surrounding medium. In the first scenario, the filaments are formed by an initially weak field that is amplified and structured by subsonic turbulent motions in a weakly magnetized medium, a scenario that has been proposed both for GC (Boldyrev & Yusef-Zadeh 2006) and the ICM environments (Porter et al. 2015; Vazza et al. 2018; Rudnick et al. 2022). The challenge in this picture is that simulations show the overall orientation of most filaments is random (Porter et al. 2015; Vazza et al. 2018). The GC filaments are mainly directed in the direction away from the Galactic plane. It is possible that the alignment of GC filaments is generated by cosmic-ray-driven wind running away from the Galactic plane, thus creating a velocity shear in the turbulent medium that aligns the filaments.

In the second scenario, the filaments are created by the subsonic flow of a weakly magnetized medium past an obstacle. The passing flow drapes the obstacle with field lines that are then compressed and stretched back into a comet-like tail, creating a magnetic filament with magnetic pressure of order the thermal ram pressure in the medium. The obstacle could be any relatively dense ionized clump that creates a bow shock in the flow such as a stellar wind bubble, a red giant, an expanding H II region, wind tubes associated with red giants in AGN relativistic bubbles (Chugai et al. 2011), or a disturbed region along jets or lobes showing size scales similar to the separation between parallel filaments. In this picture, the magnetized filaments are produced at the interaction sites of a large-scale driven wind outflowing away from the Galactic plane and embedded stellar wind bubbles (Rosner & Bodo 1996; Shore & LaRosa 1999; Yusef-Zadeh & Wardle 2019). The large-scale radio bubble filled with X-ray gas in the GC is considered to be arising from cosmic-ray-driven outflow (Yusef-Zadeh & Wardle 2019). In this picture, the obstacle sets the length scale of the separation between the filaments. This is analogous to the interaction of fast-moving mass-losing stars whose winds interact with the ISM and create cometary tails (Martin et al. 2007). In addition to the cometary model, numerous other models have been proposed in the past to explain the origin of the GC filaments and the sources in which cosmic-ray electrons are accelerated. Unlike ICM filaments, it is not clear what feeds cosmic-ray electrons into filaments (Nicholls & Le Strange 1995; Rosner & Bodo 1996; Shore & LaRosa 1999; Bicknell & Li 2001; Dahlburg et al. 2002; Yusef-Zadeh 2003; Boldyrev & Yusef-Zadeh 2006;

Ferrière 2009; Banda-Barragán et al. 2016; Yusef-Zadeh & Wardle 2019; Sofue 2020; Thomas et al. 2020; Coughlin et al. 2021).

In the context of the ICM filaments, the relative motion with the external medium is created by the orbital motion of the obstacle or a head–tail radio galaxy through the ICM around the center of the cluster. An additional contribution for slow-moving galaxies close to the center of the cluster could be moving through denser ICM (Toniazzo & Schindler 2001; Douglass et al. 2008). Other sources of external pressure could be due to "weather" motion within the ICM (Brunetti & Jones 2014). On the other hand, in the Galactic center ISM, there is a contribution due to the large-scale nuclear wind generated by high cosmic-ray pressure (Yusef-Zadeh & Wardle 2019).

One interesting aspect of this picture when applied to ICM filaments is that the filaments are linked to jets or lobes of radio galaxies. The locations where the filaments cross radio galaxies are highly distorted and cosmic-ray particles are likely to escape from the jet (Condon et al. 2021). This supports the picture in which there is a concentration of cosmic-ray particles in the jet or the lobe that injects relativistic plasma into the ICM filaments. As described in Section 4.3, the origin of filamentation is interaction with an obstacle and splitting of the filament into multiple filaments. Another possibility for the origin of the filamentation is synchrotron cooling instability formed as a result of the interaction of cosmic rays generated by the winds (e.g., Simon & Axford 1967). The mean spacing and the mean width of the filaments are expected to be similar to each other (Yusef-Zadeh et al. 2022a). In the case of ICM filaments, the spacing is estimated to be the product of the cooling timescale and the Alfvén speed which is of the order of kiloparsecs.

Assuming that the GC and ICM filaments are formed with the same mechanism in the context of an origin involving an obstacle collimating the magnetized wind, the lack of compact radio sources associated with some of the GC filaments is likely to be related to the lifetime of the obstacle. In particular, if an obstacle is an expanding H II region or a planetary nebula, then it may have already dissipated as simulations of cloud–wind interactions indicate (Banda-Barragán et al. 2016). Another possibility is that the source of injection has a very steep spectrum and would be visible only at very low frequencies.

The above cometary and turbulent models are technically different than a scenario in which there is a strong pre-existing organized field dominating the region, with only some field lines being lit up by an injected population of cosmic-ray electrons. This model was one of the first models proposed for the GC, which was originally thought to be threaded by a milligauss poloidal field (Morris 2007). However, the diffuse radio emission from the inner few hundred parsecs of the galaxy suggests a much weaker global field, $\sim$10–20 μG (Yusef-Zadeh et al. 2013). This scenario is also inapplicable to the ICM environment in which the field strengths are much less than several microgauss inferred for the magnetized filaments.

5. Summary

We compared the two populations of magnetized filaments in the GC and ICM. They differ vastly in their physical properties, such as lengths, widths, and magnetic field strengths. However, we argued that, nevertheless, they are analogous to each other as might be anticipated based on their similar morphologies.

In both cases, the filaments are in rough pressure equilibrium with their surroundings but are more strongly magnetized, consistent with scenarios in which they are formed by dynamical processes at work in their surroundings. In one scenario, which has previously been discussed in both the GC and ICM contexts, the filaments arise through the stretching and collection of field lines by turbulence in a weakly magnetized medium. An alternative scenario that has been proposed for the GC filaments is the collection and draping of field lines by a moving stellar wind source or similar obstacle with respect to the medium. It is not clear that this mechanism can create the large aspect ratios of the ICM filaments because any orbital motion is mildly transonic at best and so is unlikely to lead to a tight magnetized tail or lead to sufficient particle acceleration to energize it.

The source of the relativistic particles still remains to be established. In the GC, a few filaments have associated compact radio sources, and in the ICM the filaments are associated with radio jets and lobes, but the exact nature of any connection in both cases remains unclear. Both filament populations have steep synchrotron spectra indicating an aged cosmic-ray electron population, so it is possible that any injection event happened long ago and the link to the injecting source is no longer apparent.

The striking similarities between these enigmatic populations, despite their very different environments, suggest the possibility that one or the other may be amenable to observational probes that shed light on the physical processes at work in both populations. Some examples include (i) more sensitive MeerKAT observations of ICM sources to look for fainter as well as shorter (young and bright) filaments, (ii) high-resolution 1″ VLA study of ICM and GC filaments, and (iii) X-ray studies searching for depressions in X-ray surface brightness overlapping ICM and GC filaments.

Work by R.G.A. was supported by NASA under award No. 80GSFC21M0002. We are grateful to W. Cotton, S. Giacintucci, M. Ramatsoku, and L. Rudnick for providing the FITS images of their published data. The MeerKAT telescope is operated by the South African Radio Astronomy Observatory, which is a facility of the National Research Foundation, an agency of the Department of Science and Innovation. The National Radio Astronomy Observatory is a facility of the National Science Foundation operated under a cooperative agreement by Associated Universities, Inc.

ORCID iDs

F. Yusef-Zadeh https://orcid.org/0000-0001-8551-9220
R. G. Arendt https://orcid.org/0000-0001-8403-8548
M. Wardle https://orcid.org/0000-0002-1737-0871

References

Arendt, R. G., Staguhn, J., Dwek, E., et al. 2019, ApJ, 885, 71
Bally, J., & Yusef-Zadeh, F. 1989, ApJ, 336, 173
Banda-Barragán, W. E., Parkin, E. R., Federrath, C., Crocker, R. M., & Bicknell, G. V. 2016, MNRAS, 455, 1309
Bicknell, G. V., & Li, J. 2001, ApJL, 548, L69
Boldyrev, S., & Yusef-Zadeh, F. 2006, ApJL, 637, L101
Brienza, M., Lovisari, L., Rajpurohit, K., et al. 2022, A&A, 661, A92
Brunetti, G., & Jones, T. W. 2014, IJMPD, 23, 1430007
Chugai, N. N., Churazov, E. M., & Sunyaev, R. A. 2011, MNRAS, 414, 879
Condon, J. J., Cotton, W. D., White, S. V., et al. 2021, ApJ, 917, 18
Coughlin, E. R, Nixon, C. J., & Ginsburg, A. 2021, MNRAS, 501, 1868

Dahlburg, R. B., Einaudi, G., LaRosa, T. N., & Shore, S. N. 2002, ApJ, 568, 220
Douglass, E. M., Blanton, E. L., Clarke, T. E., Sarazin, C. L., & Wise, M. 2008, ApJ, 673, 763
Fanaroff, B., Lal, D. V., Venturi, T., et al. 2021, MNRAS, 505, 6003
Ferrière, K. 2009, A&A, 505, 1183
Giacintucci, S., Venturi, T., Markevitch, M., et al. 2022, ApJ, 934, 49
Gray, A. D., Cram, L. E., Ekers, R. D., & Goss, W. M. 1991, Natur, 353, 237
Hardcastle, M. J., Croston, J. H., Shimwell, T. W., et al. 2019, MNRAS, 488, 3416
Haynes, R. F., Stewart, R. T., Gray, A. D., et al. 1992, A&A, 264, 500
Heywood, I., Camilo, F., Cotton, W. D., et al. 2019, Natur, 573, 235
Heywood, I., Rammala, I., Camilo, F., et al. 2022, ApJ, 925, 165
Knowles, K., Cotton, W. D., Rudnick, L., et al. 2022, A&A, 657, A56
Lane, W. M., Kassim, N. E., Ensslin, T. A., Harris, D. E., & Perley, R. A. 2002, AJ, 123, 2985
Lang, C. C., Morris, M., & Echevarria, L. 1999, ApJ, 526, 727
LaRosa, T. N., Kassim, N. E., Lazio, T. J. W., & Hyman, S. D. 2000, AJ, 119, 207
LaRosa, T. N., Lazio, T. J. W., & Kassim, N. E. 2001, ApJ, 563, 163
LaRosa, T. N., Nord, M. E., Joseph, T., Lazio, W., & Kassim, N. E. 2004, ApJ, 607, 302
Law, C. J., Yusef-Zadeh, F., & Cotton, W. D. 2008, ApJS, 177, 515
Liszt, H. S. 1985, ApJL, 293, L65
Martin, D. C., Seibert, M., Neill, J. D., et al. 2007, Natur, 488, 780
Morris, M. 2007, arXiv:astro-ph/0701050
Nicholls, J., & Le Strange, E. T. 1995, ApJ, 443, 638
Nord, M. E., Lazio, T. J. W., Kassim, N. E., et al. 2004, AJ, 128, 1646
Oka, T., Geballe, T. R., Goto, M., et al. 2019, ApJ, 883, 54
Oka, T., Geballe, T. R., Goto, M., Usuda, T., & McCall, B. J. 2005, ApJ, 632, 882
Porter, D. H., Jones, T. W., & Ryu, D. 2015, ApJ, 810, 93
Pound, M. W., & Yusef-Zadeh, F. 2018, MNRAS, 473, 2899
Ramatsoku, M., Murgia, M., Vacca, V., et al. 2020, A&A, 636, L1
Rosner, R., & Bodo, G. 1996, ApJL, 470, L49
Rudnick, L., Brüggen, M., Brunetti, G., et al. 2022, ApJ, 935, 168
Shimwell, T. W., Luckin, J., Bruggen, M., et al. 2016, MNRAS, 459, 277
Shore, S. N., & LaRosa, T. N. 1999, ApJ, 521, 587
Simon, M., & Axford, W. I. 1967, ApJ, 150, 105
Sofue, Y. 2020, PASJ, 72, L4
Staguhn, J., Arendt, R. G., Dwek, E., et al. 2019, ApJ, 885, 72
Staguhn, J., Stutzki, J., Uchida, K. I., & Yusef-Zadeh, F. 1998, A&A, 336, 290
Thomas, T., Pfrommer, C., & Enßlin, T. 2020, ApJL, 890, L18
Toniazzo, T., & Schindler, S. 2001, MNRAS, 325, 509
van Weeren, R. J., Shimwell, T. W., Botteon, A., et al. 2021, A&A, 651, A115
Vazza, F., Brunetti, G., Bruggen, M., & Bonafede, A. 2018, MNRAS, 474, 1672
Yusef-Zadeh, F. 2003, ApJ, 598, 325
Yusef-Zadeh, F., Arendt, R. G., Wardle, M., et al. 2022a, ApJL, 925, L18
Yusef-Zadeh, F., Arendt, R. G., Wardle, M., et al. 2022b, MNRAS, 515, 3059
Yusef-Zadeh, F., Hewitt, J. W., & Cotton, W. 2004, ApJS, 155, 421
Yusef-Zadeh, F., Hewitt, J. W., Wardle, M., et al. 2013, ApJ, 762, 33
Yusef-Zadeh, F., Morris, M., & Chance, D. 1984, Natur, 310, 557
Yusef-Zadeh, F., & Wardle, M. 2019, MNRAS, 490, L1